Journal of Materials Chemistry A

ROYAL SOCIETY OF CHEMISTRY

PAPER

View Article Online
View Journal | View Issue

Cite this: J. Mater. Chem. A, 2023, 11, 19408

Efficient faradaic supercapacitor energy storage using redox-active pyrene- and benzodithiophene-4,8-dione-tethered conjugated microporous polymers†

Taher A. Gaber, ‡[a] Lamiaa Reda Ahmed‡[bc] and Ahmed F. M. EL-Mahdy *[ac]

Conjugated microporous polymers (CMPs) are intriguing options for a wide range of applications; however, CMP-tethered energy storage devices such as supercapacitors have received relatively little investigation due to limitations in energy density, electronic conductivity, electrochemical/structural durability, and specific capacitance. We present here the synthesis of a unique sort of redox-active conjugated microporous polymers, Py-BDT and Py-Ph-BDT CMPs, based on pyrene (Py) and redox-active benzo[1,2-*b*:4,5-*b*′]dithiophene-4-dione (BDT) units as efficient and stable electrode components for supercapacitor energy storage devices. The CMPs exhibited outstanding thermal stabilities (T_{d10}: approximately 564 °C; char yield: approximately 70.5%) and surface areas (around 427 m^2 g^{-1}). Intriguingly, integrating the pyrene and redox-active BDT units into the CMP core leads to rapid charge transport, outstanding faradaic energy storage, and remarkable conductivity. As expected, the resulting CMPs show an excellent three-electrode capacitance of 712 F g^{-1} at 0.5 A g^{-1} current density, which is a better specific capacity than that of the previously reported conventional CMPs. A symmetric two-electrode supercapacitor constructed with the Py-Ph-BDT CMP displays an effective capacitance of 429 F g^{-1} and an energy density of 38.21 W h kg^{-1} at a potential of 0.8 V and maintains 80% of its beginning capacitance over 4000 cycles. Our research provides a simple route to combine various electroactive moieties with redox-active benzodithiophene-4,8-dione to develop outstanding supercapacitors.

Received 30th May 2023
Accepted 10th August 2023

DOI: 10.1039/d3ta03198e

rsc.li/materials-a

1 Introduction

All industrial countries, economic progress, and general modernization depend on stored energy. Hence, resource depletion and energy shortages motivate scientists to explore and create energy-saving solutions.[1–4] One of the key developments to address this issue is the development of electrochemical energy storage technology.[5,6] Supercapacitors (SCs) are vital energy storage appliances owing to their good power density, enlarged cycle life, excessive charge–discharge rate, and renewability.[7] These advantageous features make SCs appropriate for various applications such as electric vehicles, wind turbines, photo flashes, machine flywheels, MP3 players, and regenerative braking systems. SCs typically store energy using two methods: faradaic processes resulting from electrode-bound bidirectional redox reactions (pseudocapacitance) and non-faradaic processes connected to the electrochemical double layer (EDL). Pseudocapacitors store energy *via* quick and repeatable faradaic redox processes on electrode surfaces, while EDL-based ones store energy through ion adsorption and desorption at the electrode–electrolyte boundary. Capacitance is enhanced in pseudocapacitors compared to those using merely the EDL.[8–10] Several factors influence the energy stored in SCs: (i) charge separation on the surface of EDL-based supercapacitors, where microporous carbon electrodes are widely used, (ii) the reaction taking place on the outermost layer of the electrode material, and (iii) interactions between electrolytes and redox-active materials.[11–14] Hence, the SC properties are profoundly influenced by the composition and chemical nature of electrode materials.[15–17] Generally, pseudocapacitors are typically constructed from transition-metal oxides such as MnO_2 and Fe_2O_3, whereas EDL-based supercapacitor electrodes are commonly constructed from various forms of carbon, such as activated carbon, graphene, and carbon nanofibers.[18–24] Organic electrode materials, including polyanilines, polypyrroles, polythiophenes, and Schiff-base polymers, appeal to some scientists due to their low energy consumption, remarkable redox activity, and environmental friendliness.[25–27] Schiff-

[a]Department of Materials and Optoelectronic Science, National Sun Yat-Sen University, Kaohsiung 80424, Taiwan. E-mail: ahmedelmahdy@mail.nsysu.edu.tw

[b]Institute of Medical Science and Technology, National Sun Yat-Sen University, Kaohsiung, 80424, Taiwan

[c]Chemistry Department, Faculty of Science, Assiut University, Assiut 71516, Egypt

† Electronic supplementary information (ESI) available. See DOI: https://doi.org/10.1039/d3ta03198e

‡ These authors contributed equally.

base polymers, for instance, can either connect redox-active moieties or serve as redox-active moieties themselves. Because different functional groups may be easily incorporated into molecules that undergo condensation, these materials are extraordinarily flexible in terms of their chemical characteristics.[28] Nonetheless, the lack of clarity surrounding most of these materials makes structural characterization and adaptation more challenging. Therefore, creating and designing tunable porous materials with massive conductivity and pseudocapacitive features architecturally is crucial to improve SC capacitance.

Organic polymers have been developed as potential candidates for the next wave of supercapacitors.[29,30] Compared to inorganic electrode materials, they have the following advantages: (i) organic polymers are typically less expensive and prevalent in nature, (ii) electrodes made from inorganic materials can only undergo single electron transfer processes, while organic polymers are capable of undergoing numerous transfer processes, and (iii) by altering their structure, organic polymers are simple to adjust their electrochemical performance, such as potential redox capacity, whereas inorganic materials present a much greater challenge.[29–33] Conjugated microporous polymers (CMPs) are developing as a significant category of organic polymers that are widely employed in SCs as vital organic electrodes because of their vast pore structure.[27,34] CMPs are covalently bonded polymers with a wide range of desirable features that include a π-conjugated core, intrinsic porosity, moderate-to-large surface area, pore diameter tunability, durability, and stability under harsh conditions; in addition, organic synthesis can change and transform their chemical structures for appropriate functionalities.[35–41] Even though CMPs have been employed in numerous fields, including photocatalysis, drug delivery, gas storage, gas separation, dye removal, and fluorescence detection, their uses as SCs electrodes are restricted by their subpar conductivity, which significantly decreases their capacitance.[42–54] CMPs are generally mixed with other conductive materials to boost the conductivity of CMP-based electrodes. Unfortunately, it is challenging to considerably improve the CMP performance due to the poor connection between the CMP and conductor.[10,27,55,56] An alternate approach for enhancing the capacitance of CMPs is to incorporate redox-active moieties, such as porphyrins, aza-fused rings, ferrocene, anthraquinone, and phenazine, into their skeletons to improve the conductivity of CMPs when they are architecturally constructed.[57–63] Even though redox-based CMPs exhibit potential redox behavior and relatively high capacitance, the variety of redox-active moieties incorporated into the skeletons of CMPs for use as innovative electrode materials is currently limited to these sorts of units. Consequently, improving supercapacitor performance requires the development of innovative redox-active CMPs with excellent conductivity and chemical durability during charge–discharge cycles.

Pyrene is a planar moiety with a fused aromatic structure and an extended π-conjugation. Owing to the potential charge-transport capability of pyrene, its derivatives have been exploited as basic components in the development of charge-transport semiconductors for application in electronic devices such as organic photovoltaic (OPV) cells and organic lasers.[64,65] On the other hand, benzo[1,2-*b*:4,5-*b*′]dithiophene-4-dione derivatives have been used to build attractive polymers in photovoltaic cells because of their potential charge-transporting and electron-donating characteristics.[66,67] To the best of our knowledge, no one has previously described the inclusion of pyrene and redox-active benzo[1,2-*b*:4,5-*b*′]dithiophene-4-dione units into the skeleton of CMPs and investigated these materials in supercapacitor applications. In this study, we describe the preparation of two redox-active pyrene- and benzodithiophene-4,8-dione-tethered CMPs (Py-BDT and Py-Ph-BDT CMPs) for energy storage application. The Py-BDT CMP was prepared through the Pt-catalyzed polycondensation reaction of 1,3,6,8-tetrakis(4,4,5,5-tetramethyl-1,3,2-dioxaborolan-2-yl)pyrene (Py-4BO, Scheme S1 and Fig. S1–S3†) with 2,6-dibromobenzo[1,2-*b*:5,4-*b*′]dithiophene-4,8-dione (BDT-2Br, Scheme S2 and Fig. S4–S6†), while 1,3,6,8-tetrabromopyrene (Py-4Br), BDT-2Br, and 1,4-phenylenediboronic acid (Ph-2BO) were utilized to prepare the Py-Ph-BDT CMP (Scheme 1). Our research showed that CMP-based electrode materials with pseudocapacitive characteristics and an outstanding specific capacity could be produced by integrating pyrene and redox-active BDT into the skeleton of CMPs. Surprisingly, the benzodithiophene-4,8-dione and pyrene-based CMPs demonstrated an outstanding specific capacity of 980 F g^{-1}, which is a better specific capacity than that of the conventional CMPs reported previously. A cyclic stability test showed that after 5000 charge–discharge cycles, 72.87% of the initial capacitance remained; such high cycle stability is rarely observed in similar materials. Moreover, BDT-based CMPs have the ability to store charge energy effectively by constructing symmetric two-electrode and three-electrode supercapacitors. Our study opens a facile avenue to connect redox-active benzodithiophene-4,8-dione with diverse electroactive moieties to produce high-performance supercapacitors.

2 Results and discussion

2.1. Materials synthesis and characterization

Through Suzuki–Miyaura coupling polymerization, two new redox-active benzodithiophene-4,8-dione- and pyrene-tethered CMPs (Py-BDT and Py-Ph-BDT CMPs) were synthesized as electrode materials for supercapacitor energy storage devices.

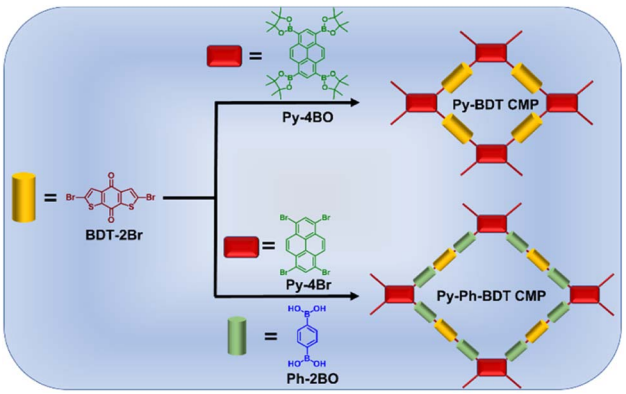

Scheme 1 Schematic synthesis of Py-BDT and Py-Ph-BDT CMPs.

Suzuki–Miyaura coupling of BDT-2Br and Py-4BO produced the Py-BDT CMP as an insoluble powder with a brown color and an 80% yield (Scheme 1 and S3†), while the Py-Ph-BDT CMP was produced as an insoluble powder with a brown color and an 81% yield through coupling between BDT-2Br, Ph-2BO, and Py-4Br (Scheme 1 and S4†). Inductively coupled plasma-atomic emission spectroscopy shows palladium impurities (0.015–0.025 mol%) in the purified Py-BDT and Py-Ph-BDT CMPs. The chemical structures and thermal stability of both Py-BDT and Py-Ph-BDT CMPs were elucidated using a variety of techniques such as Fourier transform infrared (FT-IR), solid-state ^{13}C cross-polarization (CP)/magic angle spinning (MAS) NMR, X-ray photoelectron spectroscopy (XPS), and thermogravimetric analysis (TGA). The FTIR spectrum of Py-BDT CMP lacked the bands of the C–H stretching aliphatic bond at 2923–2852 cm^{-1}, the B–O stretching bond at 1340 cm^{-1}, the C–O stretching bond at 1082 cm^{-1} and the vibration band of the C–H rocking aliphatic bond at 663 cm^{-1} for Py-4BO (Fig. 1a and S7†). The band of the C–Br stretching bond at 676 cm^{-1} related to the Py-4Br monomer was strongly mitigated in the FTIR spectrum of the product Py-Ph-BDT CMP (Fig. 1a and S8†). In addition, the vibration band corresponding to the C–Br stretching bond at 581 cm^{-1} for BDT-2Br was absent in the FTIR spectra of both Py-BDT and Py-Ph-BDT CMPs (Fig. 1a). Furthermore, the observed vibration bands of the aromatic C=C bonds, in-plane C–H aromatic bonds, and C=C–H bonds in the FTIR spectrum at 1553, 1140–954, and 852 cm^{-1} for Py-4BO, at 1593–1470, 1062–986, and 880 cm^{-1} for Py-4Br, and at 1380, 1043, 727 cm^{-1} for BDT-2Br, respectively, were shifted to 1386, 1025, and 723 cm^{-1} for the Py-BDT CMP and to 1433, 1018, and 733 for the Py-Ph-BDT CMP. In addition, the vibration band for the carbonyl C=O bond at 1653 cm^{-1} for BDT-2Br was observed to vibrate at 1652 and 1653 cm^{-1}, respectively, for the Py-BDT and Py-Ph-BDT CMPs. The vibration bands for the C–(C=O)–C stretching bond at 1261 cm^{-1} and the C–S stretching bond at 841 cm^{-1} for BDT-2Br, respectively, were clearly presented in the FTIR spectra of Py-BDT and Py-Ph-BDT CMPs at 1267 and 842 cm^{-1} for the Py-BDT CMP and at 1261 and 841 cm^{-1} for the Py-Ph-BDT CMP (Fig. 1a). The absence of signals for the C–B and C–Br carbons in the solid-state ^{13}C NMR spectra of Py-BDT and Py-Ph-BDT CMPs provided further proof that the monomers were entirely polymerized. Furthermore, the ^{13}C CP/MAS NMR spectra of both CMPs pointed out four responses at 185.24–169.44, 156.96–148.88, 147.22–137.84, and 134.90–116.55 ppm correlating to the aromatic C=O, C–S, C–C, and C–H aromatic groups for Py-BDT and Py-Ph-BDT CMPs (Fig. S9†).

We used XPS analyses to investigate the element types and their chemical states in our CMPs. Fig. S10† shows four different peaks for the O 1s, C 1s, S 2s, and S 2p orbitals for the Py-BDT CMP at 531.94, 285.94, 228.93, and 165.32 eV, respectively, and at 532.62, 285.03, 228.94, and 165.44 eV, respectively, for the Py-Ph-BDT CMP. Since there are no supplementary components in the XPS detections shown in Fig. S10,† it may be concluded that no contaminants were present during the synthesis of CMPs. We fitted the XPS patterns for the C 1s and S 2p orbitals to better understand the sorts of element species in the CMPs (Fig. 1b–e). Fig. 1b and Table S1† reveal that the C 1s orbital of the Py-BDT CMP splits into three peaks at 287.20, 285.36, and 284.40 eV, which we defined as the C=O, C–S, and C=C bonds, respectively. Additionally, the C 1s orbital of the Py-Ph-BDT CMP was split into three peaks, each corresponding to a different chemical bond: at 286.91 eV for the C=O bond, at

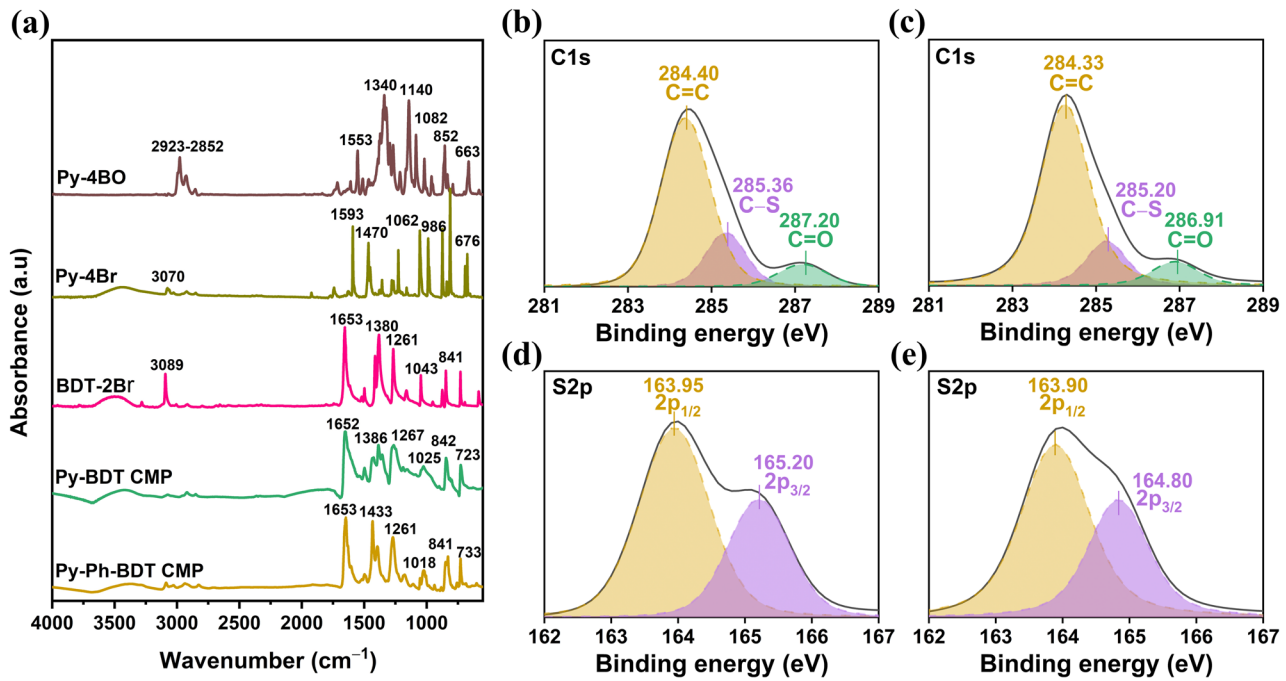

Fig. 1 (a) FTIR spectra of Py-BDT and Py-Ph-BDT CMPs and their monomers. (b–e) XPS spectra of the (b) C 1s for the Py-BDT CMP, (c) C 1s for the Py-Ph-BDT CMP, (d) S 2p for the Py-BDT CMP, and (e) S 2p for the Py-Ph-BDT CMP.

285.20 eV for the C–S bond, and at 284.33 eV for the C=C bond (Fig. 1c and Table S1†). Furthermore, two peaks at 165.20 and 163.95 eV in the S 2p orbital of the Py-BDT CMP were identified as corresponding to the two spin orbits S $2p_{3/2}$ and S $2p_{1/2}$, with a ratio of 1 : 2 (Fig. 1d and Table S1†); both of these spin orbits additionally showed up at 164.80 and 163.90 eV for the Py-Ph-BDT CMP (Fig. 1e and Table S1†).[44] The TGA measurements reveal an early weight loss of roughly 6.3% for the Py-BDT CMP and 6.4% for the Py-Ph-BDT CMP before 436 °C, which can be attributed to the desorption of the trapped solvents (Fig. S11 and S12†).[6] However, there is a mass loss of 10 wt% at temperatures of 519 and 570 °C for the Py-BDT and Py-Ph-BDT CMPs under an N_2 environment, respectively (Fig. S11, S12 and Table S2†). Notably, 70.50 and 65.13% residual masses are detected after heating to 800 °C for the Py-BDT and Py-Ph-BDT CMPs, respectively, showing that the conjugated networks have a high degree of cross-linking. Powder-XRD patterns of both Py-BDT and Py-Ph-BDT CMPs exhibited no diffraction signals, indicating that neither of these CMPs possesses long-term crystallographic properties and that both are amorphous (Fig. S13†), as has been demonstrated for previously reported CMPs.[68,69]

2.2. Porosity and morphology

We conducted gas adsorption tests using nitrogen as an absorbed material to examine the porosity properties of the Py-BDT and Py-Ph-BDT CMPs. After this, we used the Brunauer–Emmett–Teller (BET) theory to convert the original data. Fig. 2a shows type-II isotherms with steep N_2 adsorption at P/P_0 values below 0.15 and steep N_2 uptake at P/P_0 values above 0.93, originating from the micro- and mesoporous constructions of the Py-BDT and Py-Ph-BDT CMPs. In addition, we used the nonlocal density functional theory to determine the hypothesized pore dimensions of the CMPs. Fig. 2b and Table S3† show that Py-BDT CMP is a microporous material with pore sizes ranging from 1.51 to 2.63 nm, along with some mesopores having sizes between 3.54 and 6.38 nm; similarly, Py-Ph-BDT CMP is a microporous material with pore sizes ranging from 1.52 to 3.57 nm and some mesopores having sizes between 3.66 and 6.67 nm. These outcomes validated the micro- and mesopore-containing hierarchical porous topologies of the Py-BDT and Py-Ph-BDT CMPs, which are comparable to those of earlier CMPs.[70] Py-BDT and Py-Ph-BDT CMPs exhibited pore volumes of approximately 0.27 and 0.59 $cm^3\ g^{-1}$, respectively (Fig. 2b and Table S3†). The apparent BET surface areas of the CMPs range from 208 $m^2\ g^{-1}$ for the Py-BDT CMP to 427 $m^2\ g^{-1}$ for the Py-Ph-BDT CMP (Fig. S14, S15 and Table S3†). It has previously been discovered that the overall length of the framework has a significant impact on the BET surface area of porous polymers; as the length of the framework increased, the BET surface of the related polymer increased.[44] Thus, the Py-Ph-BDT CMP with a longer framework provided a higher BET surface area than the Py-BDT CMP with a shorter framework (Scheme 1). The nanoscale morphologies of our synthesized CMPs were next examined using transmission electron microscopy (TEM) and field emission scanning electron microscopy (FE-SEM). Fig. 2c–h reveal the self-assembly of both Py-BDT and Py-Ph-BDT CMPs into rod-like shapes. Statistical analysis of these TEM images revealed that the rods of Py-BDT CMP were several micrometers long and had an average width of 100–120 nm (Fig. 2c and d). The average rod width and length for Py-Ph-BDT CMP were 150–200 nm and several micrometers, respectively (Fig. 2f and g). Both Py-BDT and Py-Ph-BDT CMPs were shown to have hierarchical porous structures with pore diameters less than 10.0 nm, as evidenced by low-magnification TEM images (Fig. 2e and h), which were consistent with the outcomes of nitrogen sorption isotherms (Table S3†). FE-SEM imaging was used to validate the rod-like topologies of Py-BDT and Py-Ph-BDT CMPs (Fig. S16†). Additionally, elemental mapping using energy dispersion X-ray spectroscopy (EDS) demonstrated the existence of carbon, oxygen, and sulfur atoms in the chemical structures of Py-BDT and Py-Ph-BDT CMPs. Fig. S16b–d and f–h† indicate that the carbon, oxygen, and sulfur atoms in the structural frameworks of Py-BDT and Py-Ph-BDT CMPs were distributed uniformly.

2.3. Electrochemical properties

According to the FTIR, TGA, BET, and TEM tests, our Py-BDT and Py-Ph-BDT CMPs possessed redox-active systems, exceptional thermal durability, large surface areas, rod-like topologies, and hierarchical micro- and mesopore architectural designs, which suggests that these CMPs could be used as promising supercapacitor materials. Therefore, we first tested the electrical and electrochemical activities of these CMPs in an aqueous 1.0 M KOH electrolyte using a three-electrode system with platinum foil as the counter electrode, Hg/HgO as the reference electrode, and glassy carbon as the working electrode. The cyclic voltammetry (CV) patterns of both Py-BDT and Py-Ph-BDT CMPs at scanning intervals from 5 to 200 mV s^{-1} in the potential window of –0.7 to +0.0 V showed pseudocapacitive properties with a single predominant pair of redox peaks (Fig. 3a and b). Such redox peaks were positioned at –0.32 and –0.24 V for the Py-BDT CMP and at –0.40 and –0.37 V for the Py-Ph-BDT CMP at a scan rate of 5 mV s^{-1}. The proximity of the oxidation and reduction peaks in the CMPs indicated rapid electron transport between Py and BDT for the Py-BDT CMP and between Py, Ph, and BDT for the Py-Ph-BDT CMP. With a 40-fold boost in the rate from 5 to 200 mV s^{-1}, the positions of the oxidation peaks of the Py-BDT and Py-Ph-BDT CMPs both marginally shifted to a positive direction, whereas the reduction peaks slightly shifted to the opposite direction (Fig. 3a and b), attributing to the input impedance of the Py-BDT and Py-Ph-BDT CMPs.[71,72] Additionally, the redox peak current and the area of the accompanying CV pattern expanded as the scan speed increased; the CV patterns were able to maintain their characteristic shapes even at higher scan speeds, indicating a high-rate storage capacity and rapid kinetics of the CMPs.[63] Within a similar voltage window, galvanostatic charge–discharge (GCD) tests of Py-BDT and Py-Ph-BDT CMPs were conducted at current densities ranging from 0.5 A g^{-1} to 20 A g^{-1}. Both Py-BDT and Py-Ph-BDT CMPs showed reversed V-shaped GCD patterns with large bends, proving that they

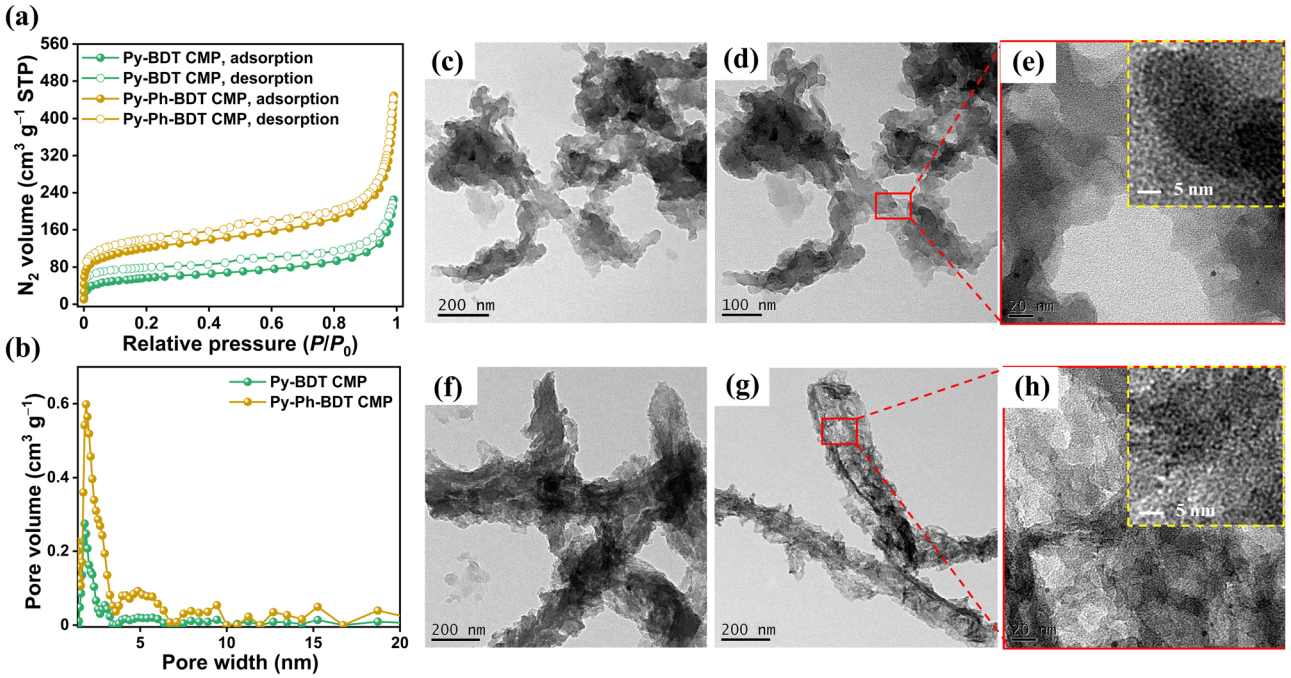

Fig. 2 (a) N_2 adsorption and desorption isotherms of the Py-BDT and Py-Ph-BDT CMPs. (b) Pore size distributions of the Py-BDT and Py-Ph-BDT CMPs. (c–h) TEM images of (c–e) Py-BDT CMP and (f–h) Py-Ph-BDT CMP. Insets: the magnified photos.

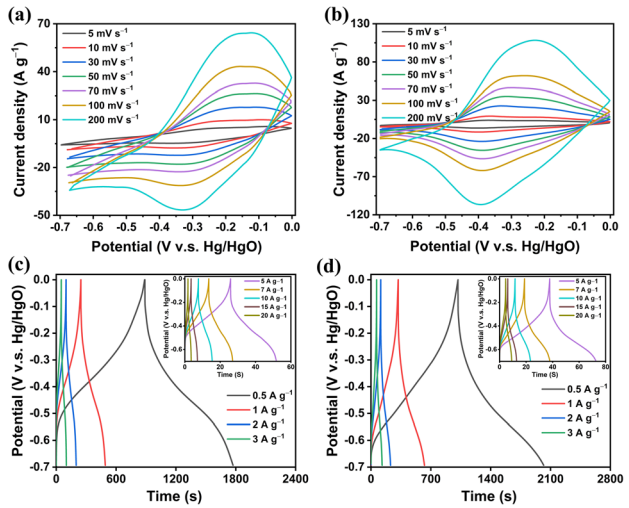

Fig. 3 (a and b) CV curves of (a) the Py-BDT and (b) Py-Ph-BDT CMPs. (c and d) GCD curves of (c) the Py-BDT and (d) Py-Ph-BDT CMPs.

behaved like pseudocapacitors (Fig. 3c and d). In general, our results revealed that integrating pyrene and redox-active BDT into the core of a CMP significantly influenced both its redox responsiveness and charge storage capacity.

The redox process of our CMPs is illustrated in Fig. 4a, which depends on the BDT monomer. The two-electron reduction of BDT into a BDT^{2-} anion is a necessary step in the redox reaction mechanism of BDT.[73] As also shown in Fig. 4a, the BDT structure was reduced using two electrons through the discharge process, whereas the reversible oxidation of the BDT^{2-} anion occurred continuously during the charge stage. Since the Py-BDT and Py-Ph-BDT CMPs have a middle surface area, a redox-active approach rather than a double-layer approach is used to manage their capacity. The GCD patterns were

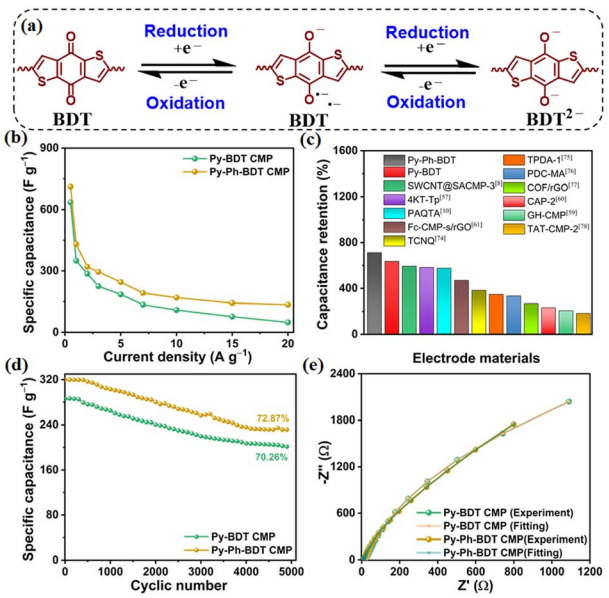

Fig. 4 (a) The suggested redox mechanism of the BDT unit. (b) Calculated specific capacitances of the Py-BDT and Py-Ph-BDT CMPs, at various current densities. (c) Comparison of specific capacitances of the Py-BDT and Py-Ph-BDT CMPs with those of previously reported redox-active porous CMPs. (d) Cycling performance of the Py-BDT and Py-Ph-BDT CMPs at a current density of 2 A g^{-1}. (e) Nyquist plots of the Py-BDT and Py-Ph-BDT CMPs and their fitted plots.

employed to calculate the specific capacitances of our CMPs. At a current density of 0.5 A g^{-1}, impressive specific capacitances of 636 and 712 F g^{-1} were obtained for Py-BDT and Py-Ph-BDT CMPs, respectively (Fig. 4b). Notably, the remarkable specific capacitances of both Py-BDT and Py-Ph-BDT CMPs surpass those of most previously reported redox-active porous CMPs such as a MWCNT/spirobifluorene (SA)-CMP (594 F g^{-1} at 1.0 A g^{-1}),[8] pyrene-4,5,9,10-tetraone (4KT-Tp)-based COF (583 F g^{-1} at 0.2 A g^{-1}),[57] polyaminoanthraquinone-triphenylamine (PAQTA)-based CMP (576 F g^{-1} at 1.0 A g^{-1}),[10] ferrocene (Fc)-based CMP/rGO composite (470 F g^{-1} at 0.5 A g^{-1}),[61] tetracyanoquinodimethane (TCNQ)-derived conductive microporous polymer (383 F g^{-1} at 0.2 A g^{-1}),[74] triazine-based porous polymer-TPDA-1 (348 F g^{-1} at 0.5 A g^{-1}),[75] triazine-based (PDC-MA) COF (335 F g^{-1} at 1.0 A g^{-1}),[76] COF/reduced graphene oxide (rGO) aerogel (269 F g^{-1} at 0.5 A g^{-1}),[77] conjugated aromatic polymer (CAP)-electrode (233 F g^{-1} at 1.0 A g^{-1}),[60] polyporphyrin-coated graphene hydrogel (GH)-CMP (206 F g^{-1} at 0.5 A g^{-1}),[59] and triazatruxene (TAT)-based CMP-2 (183 F g^{-1} at 1.0 A g^{-1})[78] (Fig. 4c and Table S4†). To our knowledge, the capacitances measured using our CMPs are the highest values ever reported for both pristine and blended CMPs. In addition, as the current density increased, the specific capacitance of both Py-BDT and Py-Ph-BDT CMPs decreased. Fig. S17† shows that specific capacitances at current densities of 5.0, 7.0, 10.0, 15.0, and 20.0 were 185, 135, 109, 77, and 49 F g^{-1} for the Py-BDT CMP and 245, 191, 169, 143, and 135 F g^{-1} for the Py-Ph-BDT CMP, respectively. This decrease in capacitance at high current density can be attributed to ohmic drop, quick and incomplete faradaic reactions, and electrolyte ion motion constraints. For charge storage, only the external active surface is employed.[79–81] Furthermore, we evaluated the Py-BDT and Py-Ph-BDT CMPs for up to 5000 cycles at a current density of 2 A g^{-1} to gauge their durability. Py-BDT and Py-Ph-BDT CMPs demonstrated remarkable electrochemical endurance by retaining 70.26% and 72.87% of their initial capacitances, respectively (Fig. 4d).

Electrochemical impedance spectroscopy (EIS) measurements were conducted at an open circuit voltage from 0.01 Hz to 100 kHz to fully analyze the charge flow impedance and diffusion rate of the constructed CMP-based electrodes and, in turn, understand the electrochemical kinetics. Fig. 4e shows the Nyquist plots of the assembled electrodes from the Py-BDT and Py-Ph-BDT CMPs. Low charge transfer impedance and substantial conductivity were demonstrated by a tiny distinctive semicircle in the high-frequency region of the CMP electrodes.[82] A virtually vertical straight line in the low-frequency region demonstrated a lower ionic diffusion barrier between the conducting electrode and electrolytic solution, indicating a diffusion-controlled electrode system.[73] In addition, at high frequencies, the curve (Fig. 4e and S18a†) is often linked to how faradaic redox capacitors with a redox-active layer relax. This is because the pseudo-redox reaction of BDT/BDT^{2-} relaxes the capacitors. A comparable circuit model (Fig. S18b†) was used to fit the EIS results, where R_s was short for the electrolyte resistance; R_{ct} stood for the resistance to charge transfer at the interface between the electrolyte and electrode, while W and CPE represented the Warburg impedance and constant phase element, respectively. Table S5† shows that R_s and R_{ct} were 17.29 and 10 586 Ω for the Py-BDT CMP and 12.09 and 6211 Ω for the Py-Ph-BDT CMP, respectively. The R_{ct} value decreased from the Py-Ph-BDT CMP to the Py-BDT CMP due to the additional phenyl unit elongated π-stacking throughout the Py-Ph-BDT CMP structure. Additionally, the Bode plots (Fig. S19†) demonstrate that the relaxation time constants of the Py-BDT and Py-Ph-BDT CMPs were 6.89 and 4.54 ms, respectively, confirming their extraordinarily strong diffusion and transport properties. These findings provided further evidence that the Py-Ph-BDT CMP-based electrode possessed a greater conductivity, which is in line with its larger capacitance value. The capacity of a supercapacitor to store energy is largely determined using several characteristics, including its energy density and power density. Ragone plots (Fig. S20†) show that at a potential of 0.7 V and a power density of 175 W kg^{-1}, the highest energy density values of Py-BDT and Py-Ph-BDT CMPs are 42.80 and 48.70 W h kg^{-1}, respectively. Therefore, by integrating the pyrene and redox-active BDT monomers into the CMP backbone, researchers could considerably enhance the capacitance and lifespan of a supercapacitor.

To better comprehend the capacitive contribution of Py-BDT and Py-Ph-BDT CMPs, we analyzed the correlation between current (i) and the scan rate (v) using the power law (eqn (1)).[83]

$$i = av^b \quad (1)$$

The slope of a plot of log(i) *versus* log(v) was utilized to determine the value of b, where a is a constant. The Py-BDT CMP had an estimated b value of 0.638 and 0.597 for the cathodic and anodic peaks, respectively (Fig. 5a), whereas the Py-Ph-BDT CMP had an estimated b value of 0.780 and 0.743 for the cathodic and anodic peaks, respectively (Fig. 5b).

These findings suggested that capacitive and diffusion-controlled energy storage operations could coexist for these two CMPs.[84] Furthermore, the increased rate capacity of the Py-Ph-BDT CMP, which may be due to its additional phenyl unit, was revealed by its greater capacitive contribution compared to the Py-BDT CMP. The capacitive contribution to total capacity was quantified using the following eqn (2):[83]

$$i(V) = k_1 v + k_2 v^{1/2} \quad (2)$$

For a fixed potential V, the total current is denoted by $i(V)$, where $k_2v^{1/2}$ and k_1v are the currents generated by the diffusion-controlled operation and capacitive effects, respectively. Fig. 5c and d show that the capacitive contributions of the Py-BDT and Py-Ph-BDT CMPs at 5 mV s^{-1} were 23% and 45%, respectively, of the total capacity. This indicates that the Py-Ph-BDT CMP has a higher capacitive contribution than the Py-BDT CMP. As the scan rate went up from 5 to 200 mV s^{-1}, the capacitive contribution increased to 59% for the Py-BDT CMP (Fig. 5c) and 86% for the Py-Ph-BDT CMP (Fig. 5d).

The structural and electrochemical variations between the Py-BDT and Py-Ph-BDT CMPs were estimated using a Gaussian 05 basis set under a density functional theory (DFT)

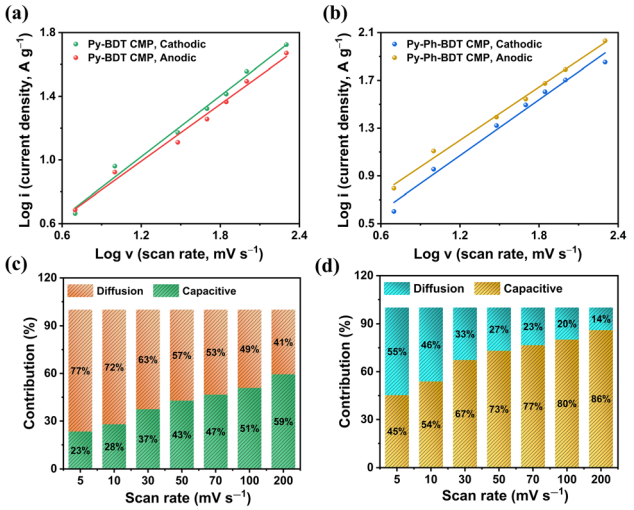

Fig. 5 (a and b) Plots of log(*i*) *versus* log(*v*) of (a) Py-BDT and (b) Py-Ph-BDT CMPs. (c and d) Relative contribution of the capacitive and diffusion-controlled charge storage of (c) Py-BDT and (d) Py-Ph-BDT CMPs, recorded at various scan rates.

approximation at a B3LYP/6-31 G* level. The appropriate geometric configurations, highest occupied molecular orbits (HOMOs), and lowest unoccupied molecular orbits (LUMOs) of the CMPs are depicted in Fig. S21.† It has been documented that the atoms with the greatest extension density of the LUMO are where the electron insertion process should take place.[85] The DFT calculations revealed that the Py, Ph, and BDT comonomers had higher ion storage and stronger electron affinity than the Py and BDT comonomers,[85] as evidenced by the electronic cloud distribution in the LUMOs (Fig. S21c and f†). The LUMO electrons of the Py-BDT CMP were localized and not spread over the entire CMP unit, whereas the Py-Ph-BDT CMP displayed a charge delocalization system with an intensely disseminated charge throughout the entire unit.

In accordance with the aforementioned findings, the higher specific capacitance of the Py-Ph-BDT CMP over the Py-BDT CMP can be attributed to the following reasons: first, the larger BET surface area of the Py-Ph-BDT CMP enabled a greater number of redox-active sites, causing an increase in specific capacity. Second, the additional phenyl unit throughout the Py-Ph-BDT CMP structure contributed to extended conjugation length and electron delocalization within the Py-Ph-BDT CMP backbone, resulting in quicker intermolecular charge transfer. Third, the higher electronic conductivity of the Py-Ph-BDT CMP permitted ultrahigh rate capabilities. Finally, the extended charge delocalization system of the Py-Ph-BDT CMP resulted in better electron mobility and greater ion storage.

To further explore the prospect for application of our CMPs in practical supercapacitor devices, a symmetric supercapacitor (SC) device of the Py-Ph-BDT CMP was constructed in a two-electrode arrangement with 1 M KOH as the electrolyte alongside the Py-Ph-BDT CMP serving as both the positive and negative electrodes and a piece of filter paper serving as the separator material (Fig. 6a). Fig. 6b displays the CV patterns of the Py-Ph-BDT CMP-tethered SC at various sweep rates between 4 and 50 mV s^{-1} in the potential run between +0.2 and +1.0 V. This figure displays quasi-reversible redox, indicating favorable capacitive activity of the electrode materials, in which the charges are primarily stored by a faradaic mechanism. It can be observed that the current density increases as the scan rate increases and the overall form of the CV curves is preserved, indicating simple kinetics and high rate capacity.[63] Fig. 6c depicts the GCD patterns of the Py-Ph-BDT CMP-tethered SC measured at varying current densities. Even at an intense current density of 10 A g^{-1}, charge–discharge patterns exhibit symmetric behaviors, suggesting that the electrochemical response is extremely reversible. Fig. 6d presents an overview of the computed specific capacitances of the Py-Ph-BDT CMP-tethered SC at various current densities based on the combined mass of one electrode. The specific capacitances of the SC at current densities of 1.0, 2.0, 4.0, 5.0, 7.0, and 10.0 A g^{-1} were 429, 386, 373, 365, 349, and 340 F g^{-1}, respectively. This result confirmed that our Py-Ph-BDT CMP-tethered SC still had a high capacitance even when the current density was high. In addition, these capacitance values exceed those of SC and asymmetric SC devices measured with equivalent redox-active electrodes (100–269 F g^{-1})[8,10,57,61,74,76,77] Fig. 6e depicts the Ragone plot of the Py-Ph-BDT CMP-tethered SC, which exhibited an outstanding energy density of 38.21 W h kg^{-1} at a potential of 0.8 V and a power density of 842 W kg^{-1}. The Py-Ph-BDT CMP-tethered SC maintained an energy density of 30.28 W h kg^{-1}, subsequent to raising the power density to 8421 W kg^{-1}. This energy density is better than those of SC and asymmetric SC devices that have been reported before based on analogous redox-active compounds, such as a MWCNT/spirobifluorene (SA)-CMP (20.6 W h kg^{-1} and 4900 W kg^{-1}),[8] conjugated aromatic polymer (CAP)-electrode (23 W h kg^{-1}),[60] pyrene-4,5,9,10-tetraone (4KT-Tp)-based COF (12.5 W h kg^{-1} and 240 W kg^{-1}),[57] ferrocene (Fc)-based CMP/rGO composite (8 W h kg^{-1} and 124 W kg^{-1}),[61] tetracyanoquinodimethane (TCNQ)-derived conductive microporous polymer (42.8 W h kg^{-1} and 8750 W kg^{-1}),[74] and triazine-based (PDC-MA) COF (29.2 W h kg^{-1} and 750 W kg^{-1}).[76] The Py-Ph-BDT CMP-tethered SC gained a good cycle duration, with 80.18% of its capacitance remaining after 4000 cycles (Fig. 6f).

Aqueous electrolytes have been regarded as attractive options because of their numerous special characteristics. However, their employment at high voltage is constrained by their limited electrochemical window (ESW, pure water 1.23 V). Organic electrolytes were used to address this shortcoming and to use a broad voltage window.[86–89] Therefore, to investigate the electrical and electrochemical activity of the Py-Ph-BDT CMP in an organic electrolyte, a symmetric supercapacitor (SC) device of this material was built using 1.0 M $TBAPF_6$/acetonitrile as the organic electrolyte. The CV patterns of the Py-Ph-BDT CMP-tethered SC with organic electrolyte are shown in Fig. S22a† for various sweep rates ranging from 1 to 20 mV s^{-1} in the potential range between +0.0 and +3.0 V. A hybrid-type supercapacitor is indicated by the observation of a quasi-rectangular shape in the CV pattern. This type of supercapacitor combines the performance of an electric double-layer capacitor with

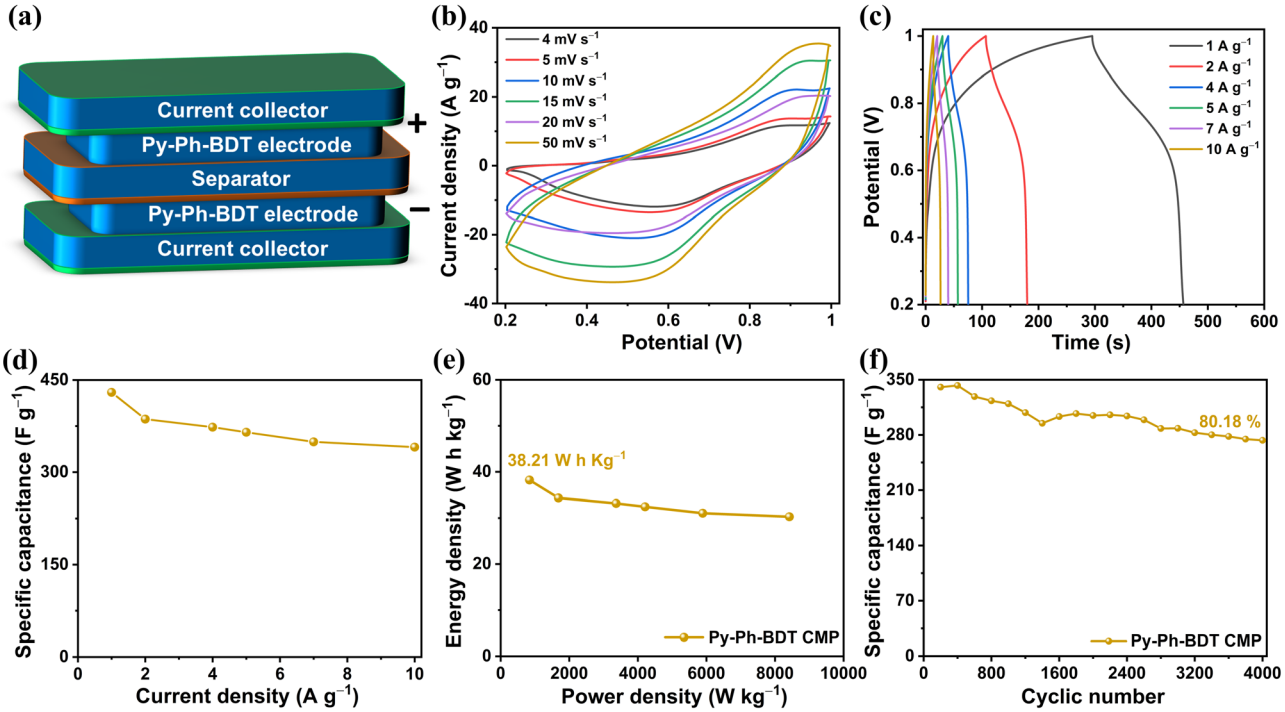

Fig. 6 (a) Fabrication of a Py-Ph-BDT CMP-tethered SC (separator is filter paper and the current collector is carbon paper). (b) CV curves of the Py-Ph-BDT CMP-tethered SC. (c) GCD curve of the Py-Ph-BDT CMP-tethered SC. (d) Calculated specific capacitances of the Py-Ph-BDT CMP-tethered SC. (e) Ragone plot of energy density *versus* power density for the Py-Ph-BDT CMP-tethered SC. (f) Cycling performance of the Py-Ph-BDT CMP-tethered SC at a current density of 5 A g^{-1}.

a pseudocapacitor. Fig. S22b† reveals the GCD patterns of the Py-Ph-BDT CMP-tethered SC with organic electrolyte measured at different current densities. The calculated specific capacitances of the Py-Ph-BDT CMP-tethered SC in the organic electrolyte at different current densities based on the mass of a single electrode are summarized in Fig. S22c.† The specific capacitances of the SC at current densities of 1.0, 2.0, 4.0, 5.0, and 10.0 A g^{-1} were 180, 161, 125, 113, and 93 F g^{-1}, respectively. Fig. S22d† depicts the Ragone plot of the Py-Ph-BDT CMP-tethered SC with organic electrolyte, which demonstrated a remarkable energy density of 225 W h kg^{-1} at a potential of 3.0 V and a power density of 3000 W kg^{-1}.

3 Conclusions

In summary, pyrene (Py) and redox-active benzo[1,2-*b*:4,5-*b*′] dithiophene-4-dione (BDT) were used as novel monomers for the synthesis of two redox-active conjugated microporous polymers, Py-BDT and Py-Ph-BDT CMPs, with outstanding thermal stabilities (T_{d10}: approximately 564 °C) and surface areas (around 427 m^2 g^{-1}). The Py-BDT CMP was synthesized through the Pt-catalyzed polycondensation reaction of Py-4BO with BDT-2Br, while Py-4Br, BDT-2Br, and Ph-2BO were utilized to prepare the Py-Ph-BDT CMP. The py and BDT units provided a vital function in inducing high-performance pseudocapacitance by enhancing the rapid charge transport, exceptional faradaic energy storage, and remarkable conductivity of the resulting CMPs. The obtained CMPs demonstrated an outstanding specific capacity of 712 F g^{-1} at 0.5 A g^{-1}, exceeding the results of previously described CMPs. A test for cycling stability revealed that up to 72.87% of the initial capacitance was still present after 5000 cycles; similar materials rarely exhibit such high cycle stability. Furthermore, a symmetric two-electrode supercapacitor fabricated with the Py-Ph-BDT CMP has an effective specific capacitance of 429 F g^{-1} and an energy density of 38.21 W h kg^{-1} at 0.8 V and 842 W kg^{-1}. This work presents a novel strategy for preparing redox-active CMPs to produce high-capacity supercapacitors.

Conflicts of interest

There are no conflicts to declare.

Acknowledgements

This study was supported financially by the National Science and Technology Council, Taiwan, under contract NSTC 111-2221-E-110-003.

Notes and references

1 Y. Tan, C. Xu, G. Chen, Z. Liu, M. Ma, Q. Xie, N. Zheng and S. Yao, *ACS Appl. Mater. Interfaces*, 2013, **5**, 2241–2248.
2 M. Ahmed, M. G. Kotp, T. H. Mansoure, R. H. Lee, S. W. Kuo and A. F. M. EL-Mahdy, *Microporous Mesoporous Mater.*, 2022, **333**, 111766.

3 K. Y. Lin and A. F. M. EL-Mahdy, *Mater. Chem. Phys.*, 2022, **281**, 125850.
4 S. Liu, L. Kang, J. Hu, E. Jung, J. Zhang, S. C. Jun and Y. Yamauchi, *ACS Energy Lett.*, 2021, **6**, 3011–3019.
5 S. Liu, L. Kang, J. Zhang, E. Jung, S. Lee and S. C. Jun, *Energy Stor. Mater.*, 2020, **32**, 167–177.
6 A. F. M. EL-Mahdy, J. Lüder, M. G. Kotp and S. W. Kuo, *Polymers*, 2021, **13**, 1385.
7 Z. Xu, S. Sun, Y. Han, Z. Wei, Y. Cheng, S. Yin and W. Cui, *ACS Appl. Energy Mater.*, 2020, **3**, 5393–5404.
8 W. Lyu, C. Yan, Z. Chen, J. Chen, H. Zuo, L. Teng, H. Liu, L. Wang and Y. Liao, *ACS Appl. Energy Mater.*, 2022, **5**, 3706–3714.
9 K. Yu, X. Pan, G. Zhang, X. Liao, X. Zhou, M. Yan, L. Xu and L. Mai, *Adv. Energy Mater.*, 2018, **8**, 1802369.
10 Y. Liao, H. Wang, M. Zhu and A. Thomas, *Adv. Mater.*, 2018, **30**, 1705710.
11 Z. Lin, E. Goikolea, A. Balducci, K. Naoi, P. L. Taberna, M. Salanne, G. Yushin and P. Simon, *Mater. Today*, 2018, **21**, 419–436.
12 T. L. Yang, J. Y. Chen, S. W. Kuo, C. T. Lo and A. F. M. EL-Mahdy, *Polymers*, 2022, **14**, 3428.
13 D. Chen, K. Jiang, T. Huang and G. Shen, *Adv. Mater.*, 2020, **32**, 1901806.
14 Y. G. Wang, Y. F. Song and Y. Y. Xia, *Chem. Soc. Rev.*, 2016, **45**, 5925–5950.
15 A. F. Saber, S. U. Sharma, J. T. Lee, A. F. M. EL-Mahdy and S. W. Kuo, *Polymer*, 2022, **254**, 125070.
16 C. Weng, X. Li, Z. Yang, H. Long, C. Lu, L. Dong, S. Zhao and L. Tan, *Chem. Commun.*, 2022, **58**, 6809–6812.
17 L. Chen, F. Wang, Z. Tian, H. Guo, C. Cai, Q. Wu, H. Du, K. Liu, Z. Hao, S. He and G. Duan, *Small*, 2022, **18**, 2201307.
18 M. B. Poudel and H. J. Kim, *Chem. Eng. J.*, 2022, **429**, 132345.
19 R. Kumar, S. Sahoo, E. Joanni and R. K. Singh, *J. Energy Chem.*, 2022, **74**, 252–282.
20 M. Athanasiou, S. N. Yannopoulos and T. Ioannides, *Chem. Eng. J.*, 2022, **446**, 137191.
21 J. Chen, J. Xie, C. Q. Jia, C. Song, J. Hu and H. Li, *Chem. Eng. J.*, 2022, **450**, 137938.
22 K. Yang, M. Luo, D. Zhang, C. Liu, Z. Li, L. Wang, W. Chen and X. Zhou, *Chem. Eng. J.*, 2022, **427**, 132002.
23 H. T. Das, S. Dutta, T. E. Balaji, N. Das, P. Das, N. Dheer, R. Kanojia, P. Ahuja and S. K. Ujjain, *Chemosensors*, 2022, **10**, 223.
24 E. Elanthamilan, A. Sathiyan, S. Rajkumar, E. J. Sheryl and J. P. Merlin, *Sustainable Energy Fuels*, 2018, **2**, 811–819.
25 Z. Sun and W. Thielemans, *J. Energy Chem.*, 2023, **76**, 165–174.
26 B. Chen and W. Y. Wong, *J. Mater. Chem. A*, 2022, **10**, 7968–7977.
27 X. Liu, C. F. Liu, S. Xu, T. Cheng, S. Wang, W. Y. Lai and W. Huang, *Chem. Soc. Rev.*, 2022, **51**, 3181–3225.
28 E. Troschke, M. Oschatz and I. K. Ilic, *Exploration*, 2021, **1**, 20210128.
29 X. Zhang, Z. Xiao, X. Liu, P. Mei and Y. Yang, *Renewable Sustainable Energy Rev.*, 2021, **147**, 111247.
30 B. Zhang, W. Wang, L. Liang, Z. Xu, X. Li and S. Qiao, *Coord. Chem. Rev.*, 2021, **436**, 213782.
31 L. R. Ahmed, C. H. Chuang, J. Lüder, H. W. Yang and A. F. M. EL-Mahdy, *Macromolecules*, 2022, **55**, 10197–10209.
32 L. R. Ahmed, L. Gilmanova, C. T. Pan, S. Kaskel and A. F. M. EL-Mahdy, *ACS Appl. Polym. Mater.*, 2022, **4**, 9132–9143.
33 K. Amin, N. Ashraf, L. Mao, C. F. Faul and Z. Wei, *Nano Energy*, 2021, **85**, 105958.
34 A. I. Cooper, *Adv. Mater.*, 2009, **21**, 1291–1295.
35 J. Chen, T. Qiu, W. Yan and C. F. J. Faul, *J. Mater. Chem. A*, 2020, **8**, 22657–22665.
36 M. G. Kotp, N. L. Torad, J. Lüder, A. A. M. El-Amir, W. Chaikittisilp, Y. Yamauchi and A. F. M. EL-Mahdy, *J. Mater. Chem. A*, 2023, **11**, 764–774.
37 S. Luo, Z. Zeng, G. Zeng, Z. Liu, R. Xiao, P. Xu, H. Wang, D. Huang, Y. Liu, B. Shao, Q. Liang, D. Wang, Q. He, L. Qin and Y. Fu, *J. Mater. Chem. A*, 2020, **8**, 6434–6470.
38 T. L. Lee, A. M. Elewa, M. G. Kotp, H. H. Chou and A. F. M. EL-Mahdy, *Chem. Commun.*, 2021, **57**, 11968–11971.
39 N. Chaoui, M. Trunk, R. Dawson, J. Schmidt and A. Thomas, *Chem. Soc. Rev.*, 2017, **46**, 3302–3321.
40 W. Zhang, H. Zuo, Z. Cheng, Y. Shi, Z. Guo, N. Meng, A. Thomas and Y. Liao, *Adv. Mater.*, 2022, **34**, 2104952.
41 J. H. Wang, T. A. Gaber, S. W. Kuo and A. F. M. EL-Mahdy, *Polymers*, 2023, **15**, 1685.
42 W. Lyu, C. Yan, Z. Chen, J. Chen, H. Zuo, L. Teng, H. Liu, L. Wang and Y. Liao, *ACS Appl. Energy Mater.*, 2022, **5**, 3706–3714.
43 M. G. Kotp, C. L. Chang and A. F. M. EL-Mahdy, *J. Water Process. Eng.*, 2023, **53**, 103675.
44 J. H. Wang, C. C. Chang, Z. W. Zhang and A. F. M. EL-Mahdy, *Polym. Chem.*, 2022, **13**, 5300–5308.
45 C. Han, S. Xiang, M. Ge, P. Xie, C. Zhang and J. X. Jiang, *Small*, 2022, **18**, 2202072.
46 A. F. Saber, A. M. Elewa, H. H. Chou and A. F. M. EL-Mahdy, *Appl. Catal., B*, 2022, **316**, 121624.
47 L. Chen, B. Chen, J. Kang, Z. Yan, Y. Jin, H. Yan, S. Chen and C. Xia, *Chem. Eng. J.*, 2022, **431**, 133222.
48 S. Luo, E. Almatrafi, L. Tang, B. Song, C. Zhou, Y. Zeng, G. Zeng and Z. Liu, *ACS Appl. Mater. Interfaces*, 2022, **14**, 39701–39726.
49 X. X. Wang, L. Liu, Q. F. Li, H. Xiao, M. L. Wang, H. C. Tu, J. M. Lin and R. S. Zhao, *Sep. Purif. Technol.*, 2023, **305**, 122517.
50 M. Shi, D. Sheng, Q. Zhuang, A. Xie and W. Dong, *ACS Appl. Polym. Mater.*, 2022, **4**, 6582–6591.
51 C. Wang, S. Ma, L. Pan, W. Wu, Y. Wei and J. Ou, *Chem. Eng. J.*, 2022, **435**, 134368.
52 C. Zhang, G. Pan and Y. He, *Talanta*, 2022, **236**, 122872.
53 K. Wang, T. M. Geng and H. Xu, *J. Appl. Polym. Sci.*, 2023, **140**, 53707.
54 Z.-S. Wu, Y. Zheng, S. Zheng, S. Wang, C. Sun, K. Parvez, T. Ikeda, X. Bao, K. Mullen and X. Feng, *Adv. Mater.*, 2017, **29**, 1602960.
55 N. An, W. Li, Z. Shao, L. Zhou, Y. He, D. Sun, X. Dong and Z. Hu, *J. Energy Storage*, 2023, **57**, 106180.

56 K. Yuan, P. Guo-Wang, T. Hu, L. Shi, R. Zeng, M. Forster, T. Pichler, Y. Chen and U. Scherf, *Chem. Mater.*, 2015, **27**, 7403.
57 M. Li, J. Liu, Y. Li, G. Xing, X. Yu, C. Peng and L. Chen, *CCS Chem.*, 2021, **3**, 696–706.
58 D. H. Roh, H. Shin, H. T. Kim and T. H. Kwon, *ACS Appl. Mater. Interfaces*, 2021, **13**, 61598–61609.
59 M. Zhang, T. Zhao, J. Dou, Z. Xu, W. Zhang, X. Chen, X. Wang and B. Zhou, *ChemElectroChem*, 2019, **6**, 5946–5950.
60 W. Liu, M. Ulaganathan, I. Abdelwahab, X. Luo, Z. Chen, S. J. Rong Tan, X. Wang, Y. Liu, D. Geng, Y. Bao, J. Chen and K. P. Loh, *ACS Nano*, 2018, **12**, 852–860.
61 A. M. Khattak, H. Sin, Z. A. Ghazi, X. He, B. Liang, N. A. Khan, H. R. Alanagh, A. Iqbal, L. Li and Z. J. Tang, *J. Mater. Chem. A*, 2018, **6**, 18827–18832.
62 Y. Kou, Y. Xu, Z. Guo and D. Jiang, *Angew Chem. Int. Ed. Engl.*, 2011, **50**, 8753–8757.
63 W. J. Sun, Y. T. Wang, Y. Zhang, B. Sun, Z. Q. Zhang, M. J. Xiao, X. Y. Li, Y. Huo, J. Xin, Q. Zhu and W. Ma, *Angew. Chem., Int. Ed.*, 2022, **61**, 202208383.
64 S. K. Nayak, R. Kore, M. S. Ahmed, P. Verma, R. Vallavoju, D. Banerjee, S. Pola, V. R. Soma, P. Chetti and S. S. K. Raavi, *Opt. Mater.*, 2023, **137**, 113603.
65 Y. Yu, P. Xu, Y. Pan, X. Qiao, L. Ying, D. Hu, D. Ma and Y. Ma, *Adv. Opt. Mater.*, 2023, **11**, 2202217.
66 H. Zhou, L. Yang, A. C. Stuart, S. C. Price, S. Liu and W. You, *Angew. Chem., Int. Ed.*, 2011, **50**, 2995–2998.
67 M. Wang, X. Hu, P. Liu, W. Li, X. Gong, F. Huang and Y. Cao, *J. Am. Chem. Soc.*, 2011, **133**, 9638–9641.
68 S. Jayanthi, D. V. S. Muthu, N. Jayaraman, S. Sampath and A. K. Sood, *ChemistrySelect*, 2017, **2**, 4522–4532.
69 R. S. Sprick, B. Bonillo, M. Sachs, R. Clowes, J. R. Durrant, D. J. Adams and A. I. Cooper, *Chem. Commun.*, 2016, **52**, 10008–10011.
70 X. H. Du, Z. Jiang, Z. Liu and C. Xu, *Microporous Mesoporous Mater.*, 2022, **332**, 11171.
71 X. Liu, C. Shi, C. Zhai, M. Cheng, Q. Liu and G. Wang, *ACS Appl. Mater. Interfaces*, 2016, **8**, 4585–4591.
72 C. Chen, M. K. Wu, K. Tao, J. J. Zhou, Y. L. Li, X. Han and L. Han, *Dalton Trans.*, 2018, **47**, 5639–5645.
73 V. V. Kondratiev and R. Holze, *Chem. Pap.*, 2021, **75**, 4981–5007.
74 Y. Li, S. Zheng, X. Liu, P. Li, L. Sun, R. Yang, S. Wang, Z. S. Wu, X. Bao and W. Q. Deng, *Angew Chem. Int. Ed. Engl.*, 2018, **57**, 7992–7996.
75 P. Bhanja, S. K. Das, K. Bhunia, D. Pradhan, T. Hayashi, Y. Hijikata, S. Irle and A. Bhaumik, *ACS Sustain. Chem. Eng.*, 2018, **6**, 202–209.
76 L. Li, F. Lu, R. Xue, B. Ma, Q. Li, N. Wu, H. Liu, W. Yao, H. Guo and W. Yang, *ACS Appl. Mater. Interfaces*, 2019, **11**, 26355–26363.
77 C. Li, J. Yang, P. Pachfule, S. Li, M. Y. Ye, J. Schmidt and A. Thomas, *Nat. Commun.*, 2020, **11**, 4712.
78 X. C. Li, Y. Zhang, C. Y. Wang, Y. Wan, W. Y. Lai, H. Pang and W. Huang, *Chem. Sci.*, 2017, **8**, 2959–2965.
79 S. A. Pande, B. Pandit and B. R. Sankapa, *Mater. Des.*, 2019, **182**, 107972.
80 A. Sarkar and G. G. Khan, *Mater. Today: Proc.*, 2018, **5**, 10177–10184.
81 S. S. Shah, S. M. A. Nayem, N. Sultana, A. J. S. Ahammad and M. A. Aziz, *ChemSusChem*, 2022, **15**, e202101282.
82 C. Young, J. Kim, Y. V. Kaneti and Y. Yamauchi, *ACS Appl. Energy Mater.*, 2018, **1**, 2007–2015.
83 Q. Li, W. Lu, Z. Li, J. Ning, Y. Zhong and Y. Hu, *Chem. Eng. J.*, 2020, **380**, 122544.
84 E. Lim, C. Jo, H. Kim, M. H. Kim, Y. Mun, J. Chun, Y. Ye, J. Hwang, K. S. Ha, K. C. Roh, K. Kang, S. Yoon and J. Lee, *ACS Nano*, 2015, **9**, 7497–7505.
85 Q. Yuan, C. Li, X. Guo, J. Zhao, Y. Zhang, B. Wang, Y. Dong and L. Liu, *Energy Rep.*, 2020, **6**, 2094–2105.
86 M. Peng, L. Wang, L. Li, Z. Peng, X. Tang, T. Hu, K. Yuan and Y. Chen, *E-Science*, 2021, **1**, 83–90.
87 W. Ni, J. Cheng, X. Li, G. Gu, L. Huang, Q. Guan, D. Yuan and B. Wang, *RSC Adv.*, 2015, **5**, 9221–9227.
88 W. Ni, D. Yang, J. Cheng, X. Li, Q. Guan and B. Wang, *RSC Adv.*, 2016, **6**, 52966–52973.
89 X. Wang, Y. Li, F. Lou, M. E. M. Buan, E. Sheridan and D. Chen, *RSC Adv.*, 2017, **7**, 23859–23865.